Pereiro-Barceló, J.; Bonet Senach, JL.; Rueda-García, L.; Ciurana-Tatay, Á. (2022). Behaviour of retrofited precast UHPC and Ni-Ti SMA column-to-foundation connection with CFRP wrapping layers. Construction and Building Materials. 323:1-17. https://doi.org/10.1016/j.conbuildmat.2022.126536

BEHAVIOUR OF RETROFITED PRECAST UHPC AND Ni-Ti SMA COLUMN-TO-FOUNDATION CONNECTION WITH CFRP WRAPPING LAYERS

Javier Pereiro-Barceló[1], José L. Bonet[2], Lisbel Rueda-García[3], Álvaro Ciurana-Tatay[4]

[1] Departamento de Ingeniería Civil (DIC), Universidad de Alicante, San Vicente del Raspeig, Carretera San Vicente del Raspeig s/n, Alicante, 46022, Spain javier.pereiro@ua.es

[2] Instituto Universitario de Ciencia y Tecnología del Hormigón (ICITECH), Universitat Politècnica de València, Valencia, Spain C/Vera s/n, Valencia, 46022, Spain jlbonet@cst.upv.es

[3] Instituto Universitario de Ciencia y Tecnología del Hormigón (ICITECH), Universitat Politècnica de València, Valencia, Spain C/Vera s/n, Valencia, 46022, Spain lisruega@cam.upv.eslisuerga@cam.upv.es

[4] Instituto Universitario de Ciencia y Tecnología del Hormigón (ICITECH), Universitat Politècnica de València, Valencia, Spain C/Vera s/n, Valencia, 46022, Spain lvaciuta@upv.es

ABSTRACT

Four precast column-to-foundation connection specimens, previously tested under lateral reversed cyclic loading and constant axial load (first-stage tests), were repaired with Carbon Fibre Reinforced Polymer (CFRP) layers in the areas where plastic hinges had formed and were retested under the same loads (second-stage tests). The columns were originally manufactured with ultrahigh-performance concrete (UHPC) with high stee-fibre content (volumetric steel/fibre ratio 1.9%). The steel bars in the connection were replaced with superelastic Ni-Ti SMA bars that crossed the column/foundation interface. Two types of connection between the precast column and the foundation were analysed: protruding bars and smooth pocket bars (SP). The specimens were subjected to the same constant level of relative axial load in both the first and second-stage tests. The objective was to determine whether the initial performance of precast UHPC and SMA reinforced column-to-foundation connections against lateral cyclic loads can be restored after a seismic event by means of simple and economic retrofitting. The effectiveness of the number of strengthening CFRP layers was also studied (two or three CFRP wrapping layers) for each column-to-foundation connection type. The main results for PB and SP connection specimens with respect to the original specimens were respectively: an average strength capacity loss of 8% and 19%, displacement ductility increase of 8% and 42%, dissipated energy 48% and 53% higher and initial stiffness 9.5%

and 21% lower. No significant differences were observed in the repairs done with two or three CFRP wrapping layers.

Keywords: UHPC, Ni-Ti, SMA, CFRP, self-centring, retrofitting, cyclic load, ductility, residual drift ratio.

HIGHLIGHTS:

- Four precast column-to-foundation connections with UHPC and Ni-Ti SMA were repaired
- The influence of the column-to-foundation connection type was studied
- Cyclic response of repaired precast columns was studied
- The effectiveness of the number of CFRP wrapping layers was analysed

1. Introduction.

Repairing damaged structures is one way to improve their sustainability and resilience. With the recent growth of composite materials, confinement of reinforced concrete elements using fibre-reinforced polymer (FRP) jackets has spread worldwide to restore structural performance. Carbon-fibre reinforced polymer (CFRP) offers good strength and durability, light weight, excellent corrosion resistance and easy construction [1]. CFRP jackets improve reinforced concrete shear strength and ductility due to the confinement it provides to lateral expansion. CFRP is then subjected to circumferential tension. The increased axial compressive and flexural strength and ultimate axial strain of the concrete core depends on several factors, among which the thickness and tensile strength of the CFRP and the compressive strength of the unconfined concrete stand out [2]. Sidiqqi et al. [3] studied experimentally the effectiveness of CFRP wraps in reducing the lateral deflections and improving the strength of slender circular reinforced concrete columns. They found that the increase in load capacity increased 71% when two CFRP layers were employed. Ferracuti et al. [4] proposed a cyclic model for square cross-sections wrapped by FRP sheets subjected to axial force and cyclic bending. The ductility increased 78% when two FRP layers were employed, 110% with three layers and 131% with six layers. Dundar et al. [5] also tested columns with different amount of FRP layers and they found that with one layer the increase in the load capacity was 27% and it was 72% with two layers. Scott et al. [6] carried out an experimental research about the seismic response of a full-scale, two-story reinforced concrete frame retrofitted by FRP jacketing. The maximum drift undergone by first story columns reduced 22%. Quiertant and Clement [7] investigated the performance of eccentrically loaded columns externally strengthened with CFRP. The strength capacity increased 30% and the deformation capacity 513% in the best case. Similar tests were carried out by Faustino et al. [8] and their results were that the load capacity rose up to 41% maintaining the ductility. Youcef et al. [9] studied slender column under compression and bending confined by CFRP layers and the bearing capacity increased 14%.

Earthquakes can cause significant deterioration of structural elements as they expose them to horizontal loads that are resisted by damaging energy-dissipation [10]. In recent years, the use of non-conventional materials has been studied to design precast structures with high seismic strength

(high energy dissipation) with high deformation and strain resistance to reduce damage to materials and residual deformation. Advanced materials such as Ultra High-Performance Concrete (UHPC) and super-elastic Nickel and Titanium (Ni-Ti) Shape Memory Alloy (SMA) bars have been used in previous studies by the authors [11–13], which showed that UHPC can stand the large strains required to develop serious stresses in SMA with excellent performance in column-to-foundation connections.

UHPC concrete has a compressive strength of at least 120 MPa at 28 days [14,15] and a flexural tensile strength up to 45 MPa [16]. Its cementitious matrix contains small metal fibres at a very high dosage rate of at least 1% by volume [15,17] which confers high ductility and reduces the need for transverse reinforcement [16,18,27,19–26]. Its use in structures dissipates energy [28] and reduces concrete damage [18,29,30] as it delays spalling of the concrete cover and compression reinforcement buckling [11,12,30]. It has also been applied to precast construction [29,31,32]. SMA bars have high ductility, can reach high strain levels and recover their predefined shape after heating or unloading. Their reversible transformation phase, or martensitic transformation give them three important structural engineering properties: the shape memory effect (SME), which makes them return to a predefined shape after heating, super-elasticity, which is the ability to recover the initial shape after unloading, and damping capacity, which is the reduction of structural movement and vibration thanks to the conversion of mechanical energy into thermal energy. Ni-Ti is the most widely used alloy and its good performance as a substitute for steel bars in structural elements in critical areas has been shown to improve their ductility and dissipate energy [33–43].

Pereiro-Barceló et al. [13] tested four precast column-to-foundation connections under cyclic loading. The columns were made with UHPC and the conventional steel bars were replaced by Ni-Ti SMA bars in the connection area. The precast columns were connected to the foundation by smooth pocket (SP) and protruding bars (PB). The specimens were tested under constant compression loads and lateral cyclic loads. The use of these materials in the connections allowed a moment-rotation behaviour with no significant damage and low residual deformations due to the super-elastic Ni-Ti SMA bars and little UHPC damage.

This paper describes the repair of the four specimens tested by Pereiro-Barceló et al. [13] with CFRP layers in the areas where plastic hinges were formed. The columns were then experimentally retested under a constant compressive load and lateral cyclic loads to study the capacity of the repaired connection to restore its original strength and deformation capacity. The aim was to determine whether the initial performance of UHPC and SMA against lateral loads in the critical regions of a precast concrete structure such as precast column-to-foundation connections can be restored after a seismic event by means of a simple and economical repair method.

2. Description and testing of the original column-to-foundation connection specimens

2.1. Original specimens

Four 260x260 mm square x 2000 mm long precast columns (Figure 1) were previously tested under cyclic loading [13] (*first test stage* hereinafter) connected to the 830x760x660 mm foundation element which was connected to a test frame by a 470-mm-long metal element. The whole assembly was pinned-pinned, and the total specimen length was 3300 mm. The behaviour of smooth pocket (SP) and protruding bars (PB) was studied. With the SP connection, the column was embedded in the foundation for 520 mm. To generate the hole in the foundation, a smooth metal pyramid-shaped formwork providing 100 mm of tolerance in each direction was used to insert the column in the connection. This space was filled with expansive mortar once the precast column had been placed and levelled. In the PB connection, longitudinal bars were anchored inside a mortar-filled 65-mm diameter sheath with a 700-mm anchorage length. An epoxy adhesive was applied to ensure contact between the upper face of the foundation and the column base. The steel and Ni-Ti SMA reinforcement arrangement is shown in Figure 1.

A relative normal force ($\nu = N/(b \cdot h \cdot f_c)$ (where N is the applied axial load, b is the cross-section width, and f_c is the average concrete compressive strength of the column) of 0.20 was applied in all the tests.

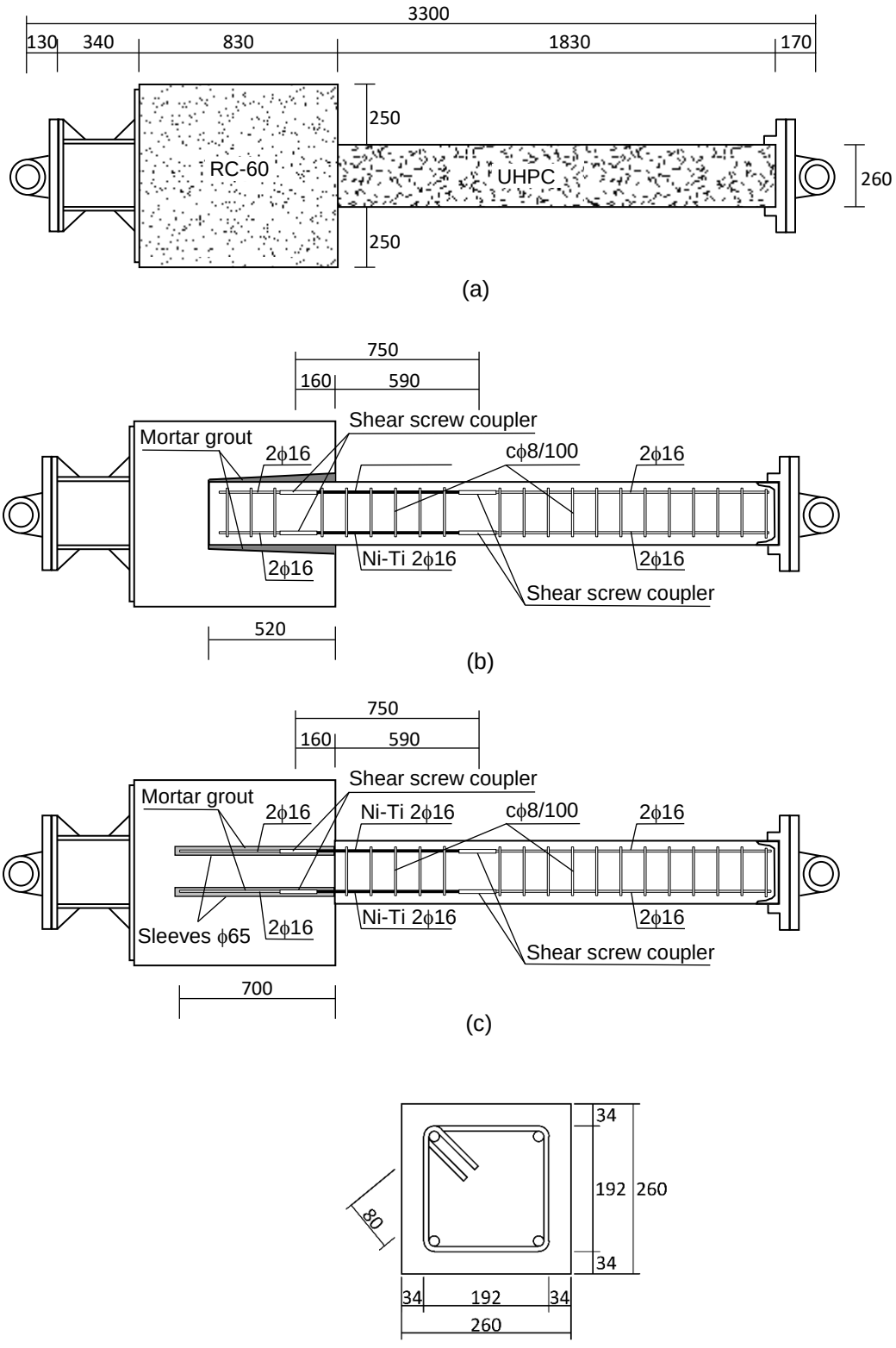

Figure 1: Dimensions and reinforcement of the test specimen (unit: mm): (a) dimensions; (b) smooth pocket; (c) protruding bars; (d) cross-section details

Table 1 details the four specimens in the first stage of the test, where b and h are the dimensions of the cross section, λ_V is the shear slenderness, s_t is the stirrup separation and ν is the relative axial

load. Designation of the as-built specimens was by using Zx-YYV02 ("x" indicates specimen number and "YY" the connection type, PB for protruding bars and SP for smooth pocket) and V02 the relative axial load (in this case the value for all specimens was 0.2). Two specimens were tested per connection type to analyse the dispersion of the experimental results.

Table 1: Details of the as-built test specimens (first stage).

Id Specimen	Age at testing (since the precast column was built), days	b (mm)	h (mm)	λ_V	s_t (mm)	Connection type	Axial load (kN)	ν
Z1-PBV02	33	260	260	7.69	100	Protruding bars	1627.81	0.20
Z2-PBV02	27	260	260	7.69	100	Protruding bars	1710.28	0.20
Z3-SPV02	28	260	260	7.69	100	Smooth pocket	1646.74	0.20
Z4-SPV02	30	260	260	7.69	100	Smooth pocket	1644.03	0.20

2.2. Materials

Table 2 indicates the average compressive strength of the grout mortar according to UNE-EN 12390-3:2020 [44] used in the column/ foundation connection. In this case four concrete cubes (100 mm side) were taken. The materials were characterised on the same day as the as-built specimen was tested (first test stage). The properties of the materials employed in the foundation, precast columns and the characterization of the mortar grout are depicted in Table 2, where f_c is the average concrete compressive or mortar strength, E_c is the concrete or mortar modulus of elasticity, f_{LOP} is the limit of proportionality in the flexural tensile strength test and $f_{R,j}$ are the residual tensile strengths that corresponded to the Crack Mouth Opening Displacement (CMOD) of 0.5, 1.5 and 2.5 mm [45].

Table 2: Mechanical properties of the as-built test specimen concretes.

Id Specimen	Foundation		Column						Mortar grout
	f_c (MPa)	E_c (MPa)	f_c (MPa)	E_c (MPa)	f_{LOP} (MPa)	f_{R1} (MPa)	f_{R2} (MPa)	f_{R3} (MPa)	f_c (*) (MPa)
Z1-PBV02	70.35	41746	120.4	42256	14.03	23.12	22.03	19.25	53.02
Z2-PBV02	48.51	39785	126.5	46519	10.15	17.71	16.87	13.82	52.56
Z3-SPV02	67.09	39675	121.8	42506	14.19	25.01	26.98	22.79	51.92
Z4-SPV02	61.03	39560	121.6	42324	12.25	21.34	21.46	18.33	52.04

(*) Concrete cube 100x100x100 mm

The steel was B 500 SD (EHE-08 [46]) and C class (EC-2 [47]).

Figure 2 shows the stress-strain curve of the characterisation of steel reinforcements according to UNE-EN 10002:1:2002 [48]. In this figure, f_y, ε_y, f_{sh}, ε_{sh}, f_u, ε_u and E_s, are the yield strength of the reinforcement, reinforcement strain at yield strength, stress at which the hardening branch begins, strain associated with f_{sh}, reinforcement tensile strength, strain associated with tensile strength and the modulus of elasticity, respectively. The shown values are the average of two characterisation tests on each bar diameter.

The Ni-Ti SMA bars were 16 mm in diameter with a polished surface. The four transformation temperatures were determined by differential scanning calorimetry (DSC) (A_s and A_f for the beginning and end of austenitic transformation, M_s and M_f for the beginning and end of martensitic transformation) according to Standard ASTM F2004-05 (2010) [49]: M_f = -53.74°C, M_s = -28.47°C, A_s = -27.99°C and A_f = -5.34°C.

Figure 2 depicts the stress-strain curve of the tensile Ni-Ti SMA bars. The austenitic modulus E_A equalled 66586.41 MPa, martensitic modulus E_M was 2892 MPa, martensitic transformation initial stress f_A was 464.20 MPa for a strain ε_A of 7.1‰, and the martensitic transformation end stress f_M was 650.50 MPa for a strain ε_M of 71.3‰. The test room temperature was set at 20-25°C.

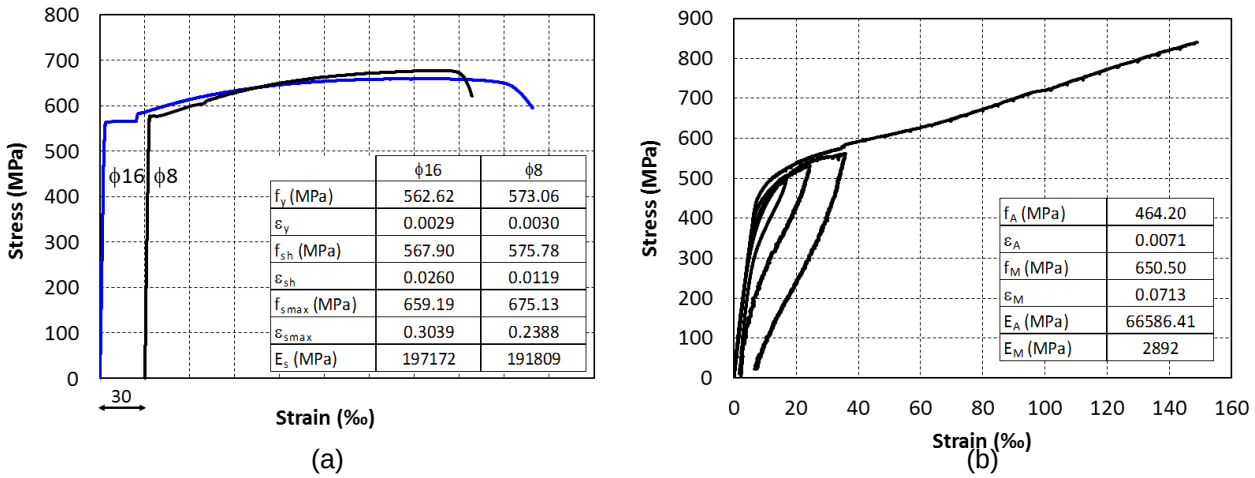

Figure 2: Mechanical properties of reinforcements: (a) steel reinforcements, (b) SMA reinforcements.

3. Experimental programme of the repaired specimens.

3.1. Repairing the damaged specimens.

After the first test stage the damaged concrete was removed, cracks were filled with an epoxy resin, an ultrahigh-performance repair mortar was used to rebuild the cross-section and the columns were strengthened with two or three layers of CFRP wrapping. The specimens were tested in a second stage with the same reduced axial load as the as-built specimens ($\nu = 0.20$). Table 3 shows the details of the four repaired specimens included in the experimental programme along with the identifier of the as-built specimen. The repaired specimens were designated ZxR-YYV02-nL, where "x" indicates the specimen number, "YY" the connection type (PB for protruding bars and SP for smooth pocket) and "n" the number of CFRP layers.

Table 3: Details of the repaired test specimens (second test stage).

Id repaired specimen	Id as-built specimen	CFRP layers	Age at testing (since the precast column was built), days	Axial load (kN)	ν	Repair mortar		
						Age at testing (days)	$f_{c,mortar}$ (MPa)	$E_{c,mortar}$ (MPa)
Z1R-PBV02-2L	Z1-PBV02	2-layer CFRP	111	1627.81	0.20	28	111.00	44525
Z2R-PBV02-3L	Z2-PBV02	3-layer CFRP	100	1710.28	0.20	28	126.50	45530
Z3R-SPV02-2L	Z3-SPV02	2-layer CFRP	110	1646.74	0.20	28	126.50	45530
Z4R-SPV02-3L	Z4-SPV02	3-layer CFRP	120	1644.03	0.20	28	126.50	45530

Figure 3 depicts the critical zone of the four specimens after removing damaged concrete. As can be seen, the damage in the critical zone depended on the type of connection with the foundation. The specimens with a PB connection (Z1R-PBV02 and Z2R-PBV02) had further reduced damage, which was concentrated at the column/foundation joint at a distance of between 50 and 100 mm (Figure 3.a and b). However, the section at the interface between the column and the foundation remained undamaged in the specimens connected by an SP type connection (Z3R-SPV02 and Z4R-SPV02). The most seriously damaged area was around the main crack in the column, with damage reaching up to 200 mm from the top of the foundation (Figure 3.c and d).

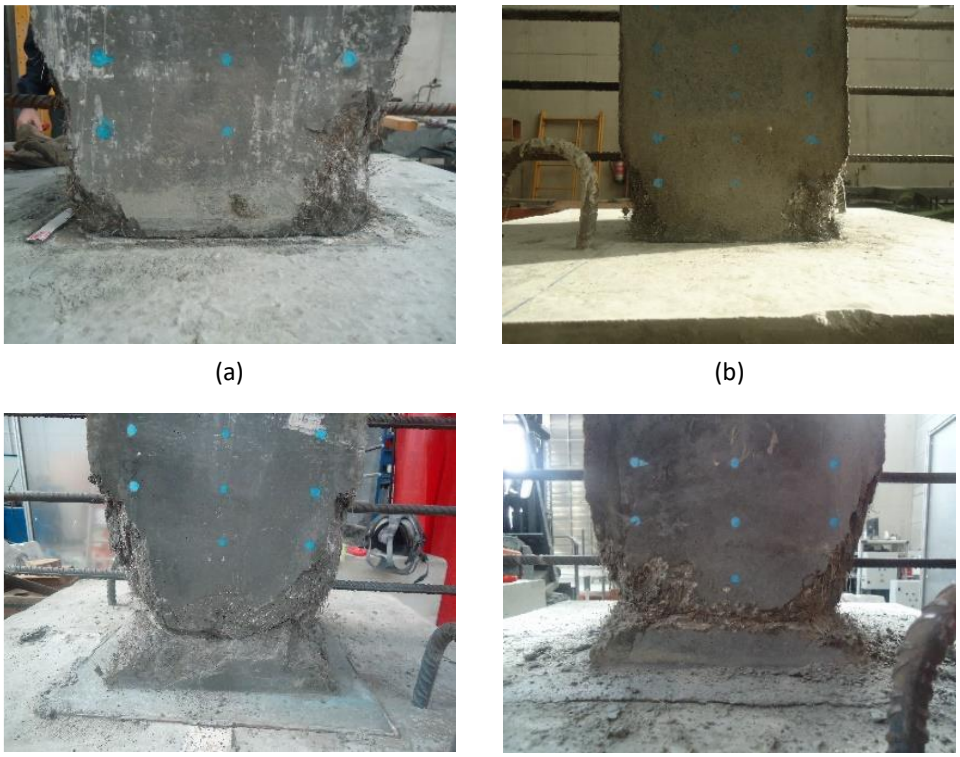

Figure 3: Column damage: (a) specimen Z1R-PBV02-2L; (b) specimen Z2R-PBV02-3L; (c) specimen Z3R-SPV2-2L; (d) specimen Z4R-SPV02-3L.

After removing the damaged concrete, both the joint between the column and the foundation in the specimens with a PB bar connection (Z1R-PBV02-2L and Z2R-PBV02-3L) and the main crack in the column in the specimens with a SP-type connection (Z3R-SPV02-2L and Z4R-SPV02-3L) were sealed with high-strength and low-viscosity epoxy resin (Sikadur®-52). The manufacturer's mechanical properties were as follows: elasticity modulus 1800 MPa, compressive strength 52 MPa, tensile strength 37 MPa and flexural tensile strength 61 MPa (Figure 4.a and b).

The damaged area was then repaired with ultrahigh-performance repair mortar (Figure 4.c) with a similar elasticity modulus to that of the UHPC concrete to ensure strain compatibility between the mortar and the existing UHPC. The mortar dose was: 1000 kg/m^3 of Portland Cement type CEM I 42.5 R, 310 kg/m^3 of sand 0/4, 575 kg/m^3 of sand 0/8, 150 kg/m^3 of silica fume, 170 kg/m^3 of water and 29 kg/m^3 of fluidiser (Sika Viscocrete®-20 HE). Table 3 shows the results of the average compressive strength ($f_{c,mortar)}$ and the modulus of elasticity ($E_{c,mortar)}$ of the mortar, according to UNE-EN 12390-3:2020 [44] and UNE-EN 12390-13:2014 [52]. Three cylinders (300 mm high, 150 mm diameter) were taken from each specimen.

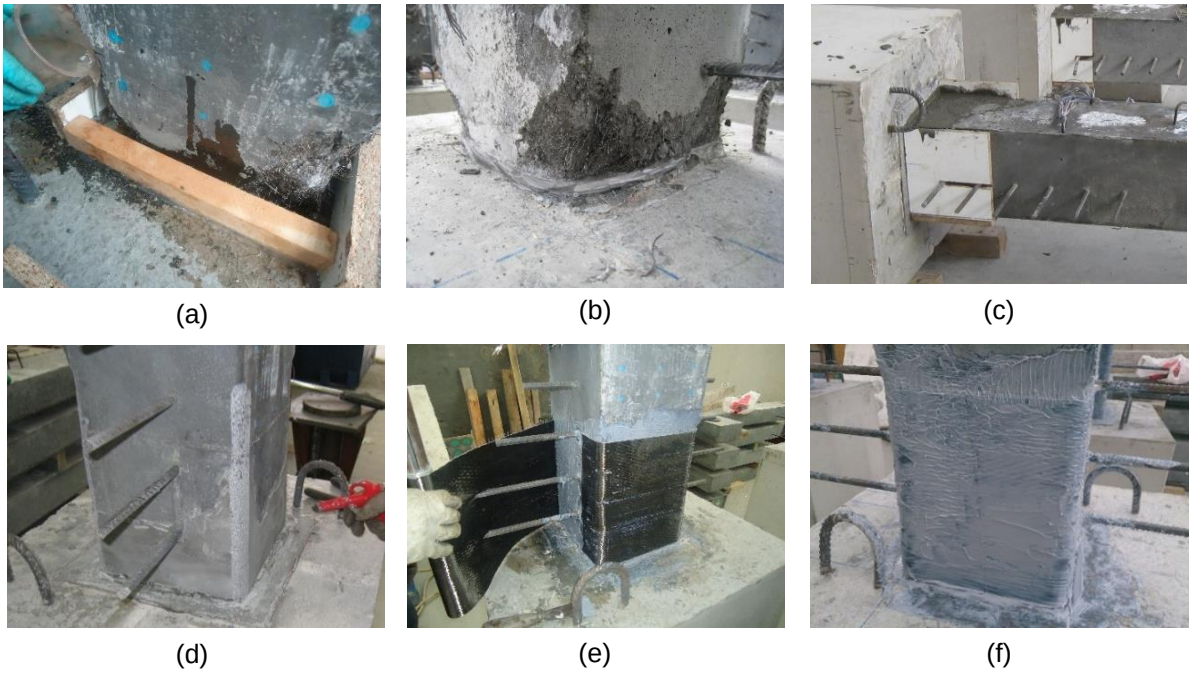

(a) (b) (c)

(d) (e) (f)

Figure 4: Repairing specimen Z2R-PBV02: (a) pouring resin; (b) sealed column-to-foundation joint; (c) casting the repair mortar; (d) state of repair after rounding corners; (e) carbon fibre placement; (f) final state after repair.

The corners of the columns were rounded off to a radius of 20 mm (Figure 4.d) to provide effective CFRP wrapping confinement. Al-Saloum [53] found that the confinement effectiveness of this wrapping in a rectangular column decreased as a result of the stresses concentrated in the corners of the cross-section and broke the CFRP. The sheets were wrapped with an application length of 300 mm from the column/foundation interface (Figure 5).

A repair system that combined epoxy resin adhesive (Sikadur®-330) with a unidirectional carbon fibre fabric (SikaWrap®-230C) was then applied. The fibres were oriented transversely to the specimen axis to improve concrete confinement. The mechanical properties were provided by the manufacturer: laminate tensile strength of CFRP sheets 3500 MPa, laminate tensile elasticity modulus 225 GPa, thickness of 0.129 mm and laminate elongation at break in tension 1.56%. Figure 4.e and f show the placing of the CFRP sheets and the final state of repair.

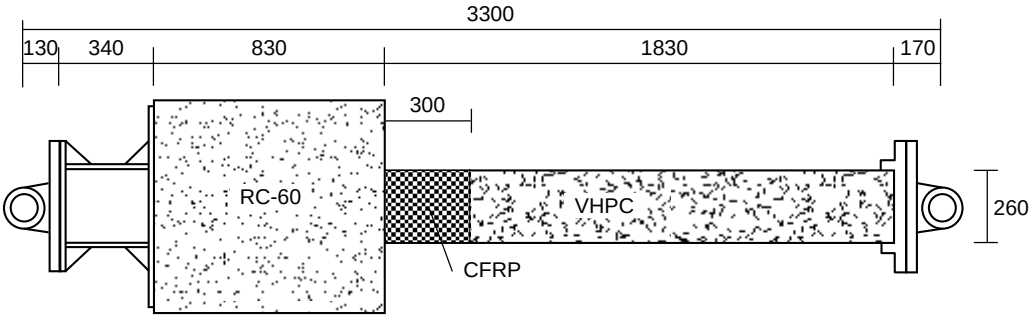

Figure 5: Dimensions of repaired test specimen (unit: mm).

3.2. Test setup, instrumentation and test procedure.

The repaired specimens were tested in a second stage under lateral reversed cyclic loading and constant axial load in a custom-made steel-loading frame, as shown in Figure 6.a. As in the first stage, the test room temperature was set at 17-18°C, as were the loads applied to the repaired specimens. A horizontal load equal to the relative normal force was first applied and remained constant throughout the test by means of a 2500 kN hydraulic actuator (Figure 6.b). The lateral load was then applied with displacement control at a constant velocity of 0.2±0.05 mm/min by means of a 500 kN double-effect hydraulic jack (Figure 6.c). The test sequence of the displacement-controlled cycles is expressed in terms of drift ratio (Δ/L_s). Three complete cycles were applied for each drift ratio (0.5, 0.75, 1, 1.5 ,2, 2.5 , 3 etc) , as defined in ACI 374.1[54], FEMA-356 [55] and P-750-FEMA [56]. The drift ratio Δ/L_s is obtained by dividing the Δ displacement at the end of the column in each direction by the length of column L_s. The earthquake effect was simulated by applying this quasi-static lateral load in incremental displacement cycles [57]. Figure 7 shows the calculation of the Δ displacement at the end of the column.

The instrumentation on the specimens is shown in Figure 8. These included twenty-seven linear variable differential transformers (LVDTs). Devices 1-11 recorded the lateral displacement (Figure 8.a). The foundation rotation was obtained by devices 10 and 11. Devices 11-23 (Figure 8.b) were designed to indirectly record the average bending curvature at six sections from the column/foundation interface. In the specimens with a protruding bar type connection, four LVDTs (devices 24-27) recorded possible joint displacements (Figure 8.c).

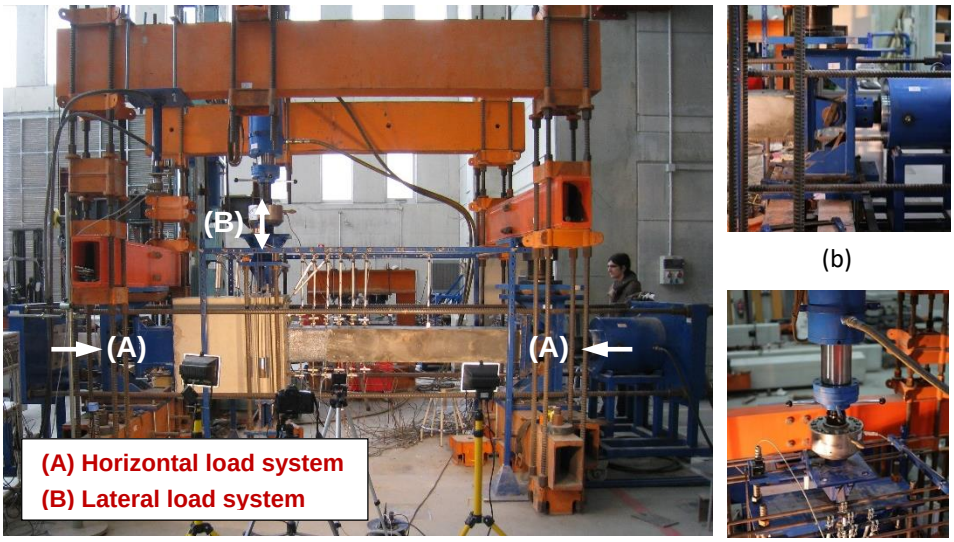

Figure 6: The outer test configuration: (a) global set-up; (b) hydraulic actuator that applied the axial load; (c) hydraulic actuator that applied the lateral load.

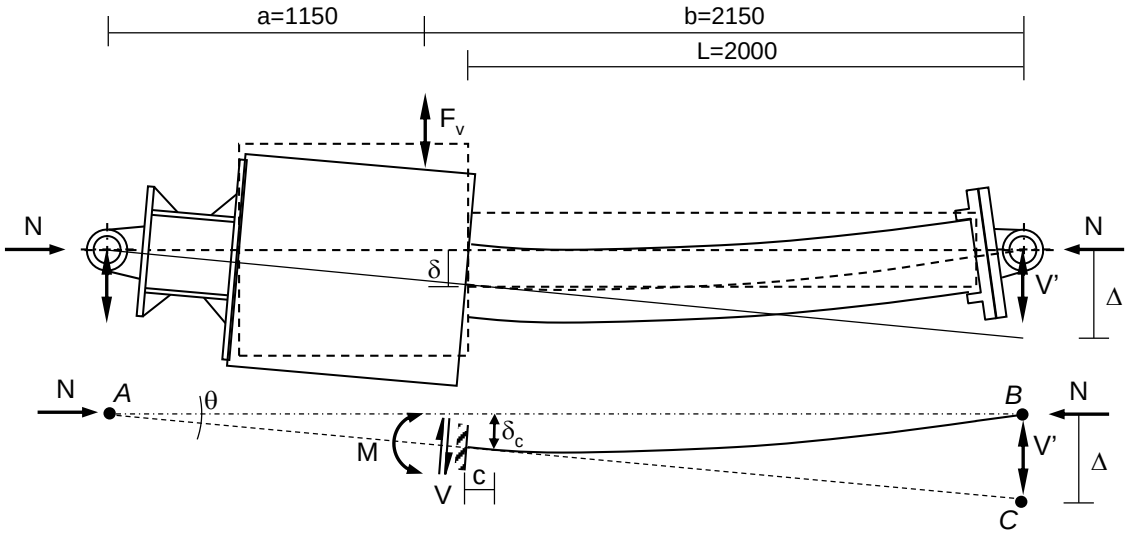

$$V' = F_v \frac{a}{a+b}; \quad \Delta = \delta \frac{a+b}{L}; \quad \theta = \Delta/(a+b); \quad V = V' cos\theta - N sin\theta$$

$$M(x=c) = N \cdot \delta_c + V' \cdot (L-c)$$

Figure 7: Idealised specimen.

A synchronised recording system was used in which each photogram was assigned to the corresponding applied load. The forces applied to the specimens by hydraulic actuators were controlled by two load cells: a 2000 kN cell attached to a plate inside the horizontal loading system frame, and a 500 kN cell between the specimen and the lateral load hydraulic actuator.

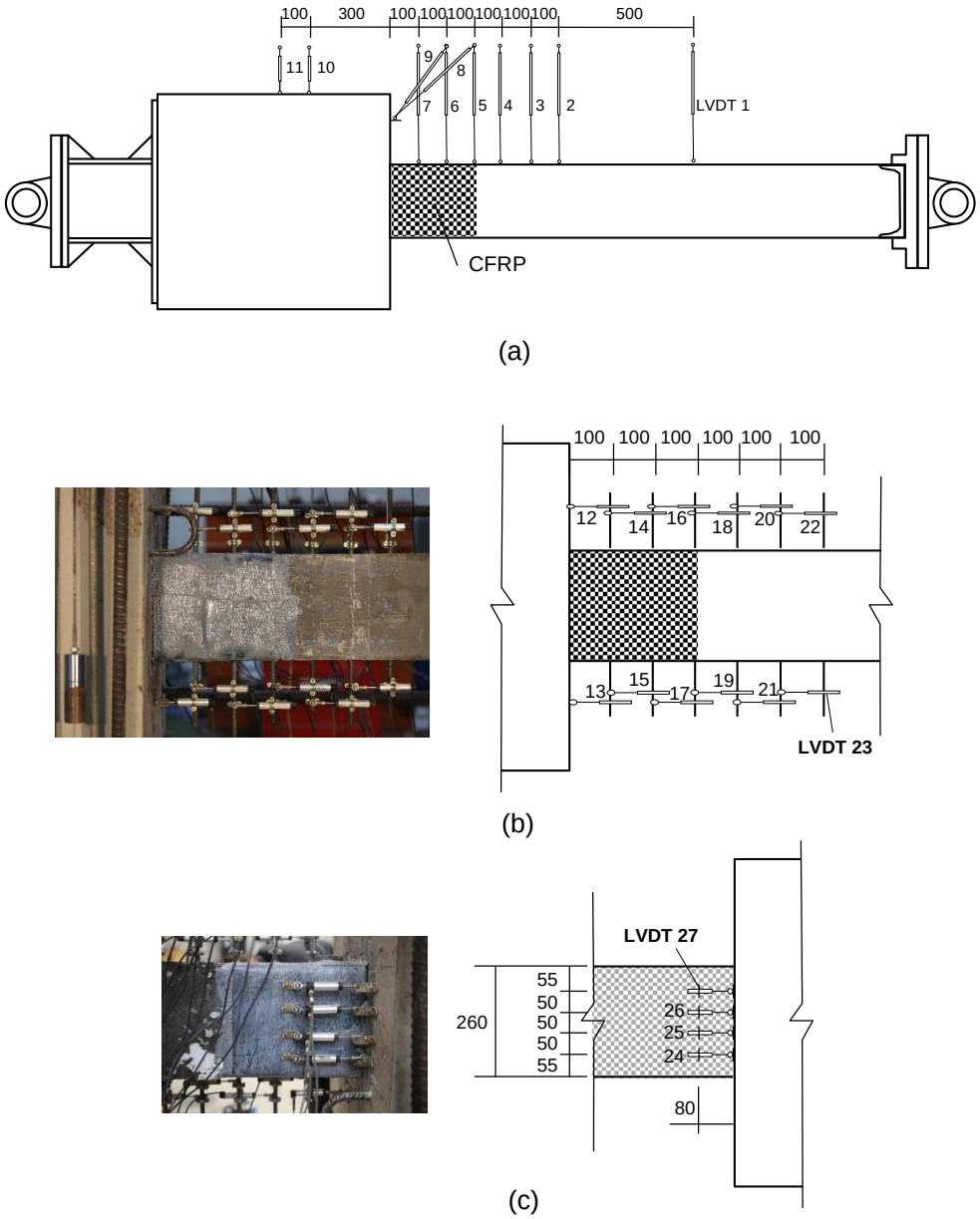

Figure 8: LVDT arrangement (unit: mm): (a) Vertical LVDTs in the connection; (b) Horizontal LVDTs in the connection; (c) LVDTs in the joint of the specimens with a protruding bar type connection.

3.3. Test observations of the repaired specimens.

Figure 9 depicts the behaviour of the specimens for a drift ratio (Δ/L_s) of approximately 5%, where the shear force (V) was practically zero and there was at least a 20% lateral load (V') loss (Figure 7). Figure 10 depicts column damage at the end of the tests after removing the CFRP sheets. The following general observations were made:

1. The effectiveness of the confinement provided by the repair by CFRP wrapping in the four tested specimens prevented cover spalling of the repair mortar and the confinement prevented the Ni-Ti compressed bars from buckling. There was neither local failure in the bond zone between concrete and the CFRP wrapping (debonding) nor did the layers separate in the laminate due to adhesive failure (delamination).

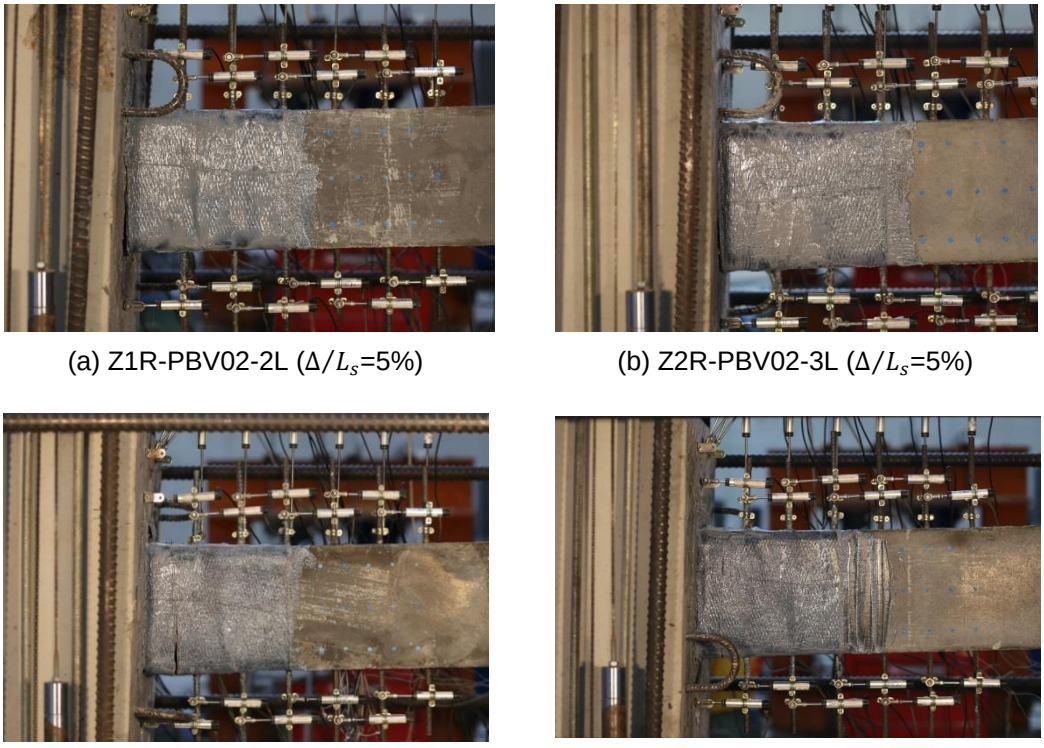

(a) Z1R-PBV02-2L (Δ/L_s=5%) (b) Z2R-PBV02-3L (Δ/L_s=5%)

(c) Z3R-SPV02-2L (Δ/L_s=5%) (d) Z4R-SPV02-3L (Δ/L_s=5%)

Figure 9: Repaired specimen appearance at ultimate (second test stage).

2. As found in the first test stage, rocking behaviour took place in the joint between the column and the foundation in the specimens with the PB connection type (Z1R-PBV02-2L and Z2R-PBV02-3L) (Figure 9.a and b) due to loss of adhesion between the Ni-Ti SMA bars and UHPC because the tensile strain required by the gap opening was not concentrated on the joint but was distributed along the entire length of the Ni-Ti SMA bars. The confinement provided by the CFRP wrapping allowed both the UHPC and high-strength mortar to achieve high strains without crushing (Figure 10.a and b). No broken CFRP wrapping was detected in the repaired area. In the Z1R-PBV02-2L specimen bulging occurred at the end of the test on one specimen lateral face at a distance of 100 mm from the joint. As at the end of test of specimen Z2R-PBV02-3L, there was slight noise due to breakage of the epoxy resin of the CFRP wrapping transversely to the specimen axis. In these specimens,

both the super-elastic Ni-Ti SMA bars and the slight damage to both UHPC and mortar confined by the CFRP wrapping reduced residual deformation.

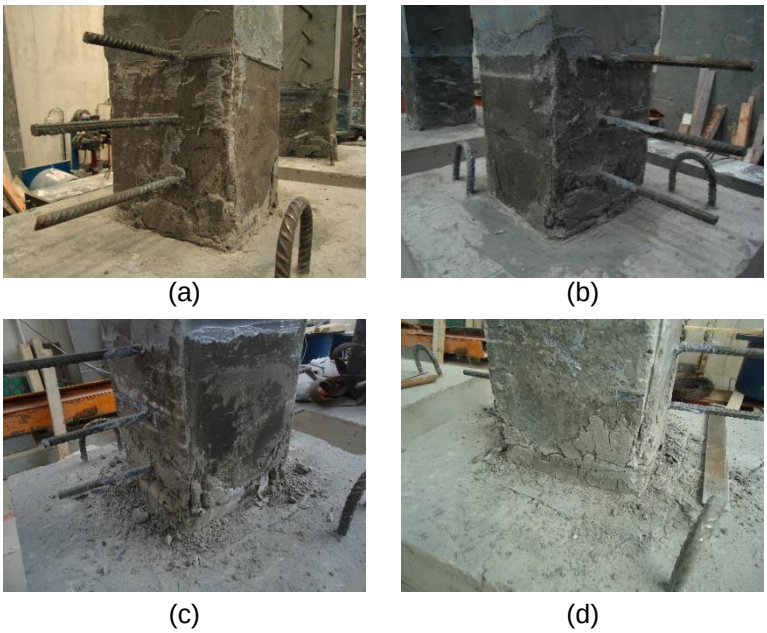

Figure 10: Column damage at the end of the second stage after removing the CFRP sheets.

3. Continuous sounds were heard from the epoxy resin transversal breakage in the specimens with an SP connection (Z3R-SPV02-2L and Z4R-SPV02-3L). This failure produced a visible bending crack in the column in a critical section approximately 60-70 mm from the column/foundation interface in approximately the same position of the main crack in the as-built specimens. The crack opening in specimen Z3R-SPV02-2L was wider than in specimen Z3R-SPV02-3L (Figure 9.c and d). Once the crack had formed, rocking behaviour occurred at the critical section as in the as-built specimens (first test stage). In the final stage of specimen Z3R-SPV02-2L, a crack appeared in the lower column 15 mm from the interface, also a bulge 15 mm from the interface on the upper column and 175 mm from the interface on the bottom and sides. This allowed the cracks in the section to widen under the CFRP because of the lack of confinement. Similarly, in the final stage of specimen Z4R-SPV02-3L bulging occurred on the sides 100 mm and 200 mm away from the column/foundation interface. The specimen with two CFRP wrapping layers (Z3R-SPV02-2L) obtained greater damage than the repair with three CFRP wrapping layers (Z4R-SPV02-3L), which led to greater confinement loss in specimen Z3R-SPV02-2L and led to more marked concrete

crushing (Figure 10.c and d). The limited damage to concrete and mortar together with the super-elastic Ni-Ti SMA bars meant the minimum residual deformations in the specimens.

4. The SP connection specimens underwent more damage than the PB ones for the following reasons: (1) the main bending crack appeared in the critical zone of the SP connection; (2) the breakage of the epoxy resin near the bending crack in the SP connection reduced the confinement of the CFRP wrapping; (3) for high drift ratios, the bulging of the CFRP wrapping made wider cracks in the SP connection; (4) deformation capacity was concentrated at the column-foundation joint in the PB connection (rocking behaviour), which reduced the damage and prevented cracking. This rocking was due to: (1) adequate CFRP confinement of both the concrete and the repair mortar; (2) the deformation capacity of the polished Ni-Ti SMA bars; (3) the bond loss between the UHPC and Ni-Ti SMA bars.

5. The critical section in the specimens with a PB connection (Z1R-PBV02-2L and Z2R-PBV02-3L) was thus at the joint of the column with the foundation; i.e. $c = 0$ (Figure 7). In SP-connected specimens, the critical section moved from the spot where the column and the foundation met to a distance of $c = 70\ mm$ (position of the main crack on the column), as in the as-built specimens (first test stage).

4. Results and Discussion.

4.1. Test results.

As Liu (2013) [58] stated, when lateral deflection Δ and applied axial load N are large, the difference between the lateral shear force (V) and the applied lateral load (V') can be significant (Figure 7). All the figures of these Sections represent the vertical shear force (V).

Figure 11 shows the experimental results for the shear force V-Drift ratio of the as-built specimens (first test stage) compared to the repaired specimens (second test stage). The maximum shear force in all the specimens, was reached accompanied by a descending post-peak branch. Figure 12 provides the experimental results of the total bending moment-average curvature at the critical section of both the as-built and repaired specimens. This moment was obtained as the sum of a primary moment caused by the applied lateral cyclic load (V') and a secondary moment caused by

the applied axial load N. The critical section in the specimens with a PB connection was at the joint between the column and the foundation, where the moment was longest, the critical section was displaced t0 a distance of $c = 70\ mm$ from the foundation in the SP specimens, as indicated by the most seriously damaged region (Figure 7). The average curvature was obtained from the readings of LVDTs 12 and 13 (Figure 8).

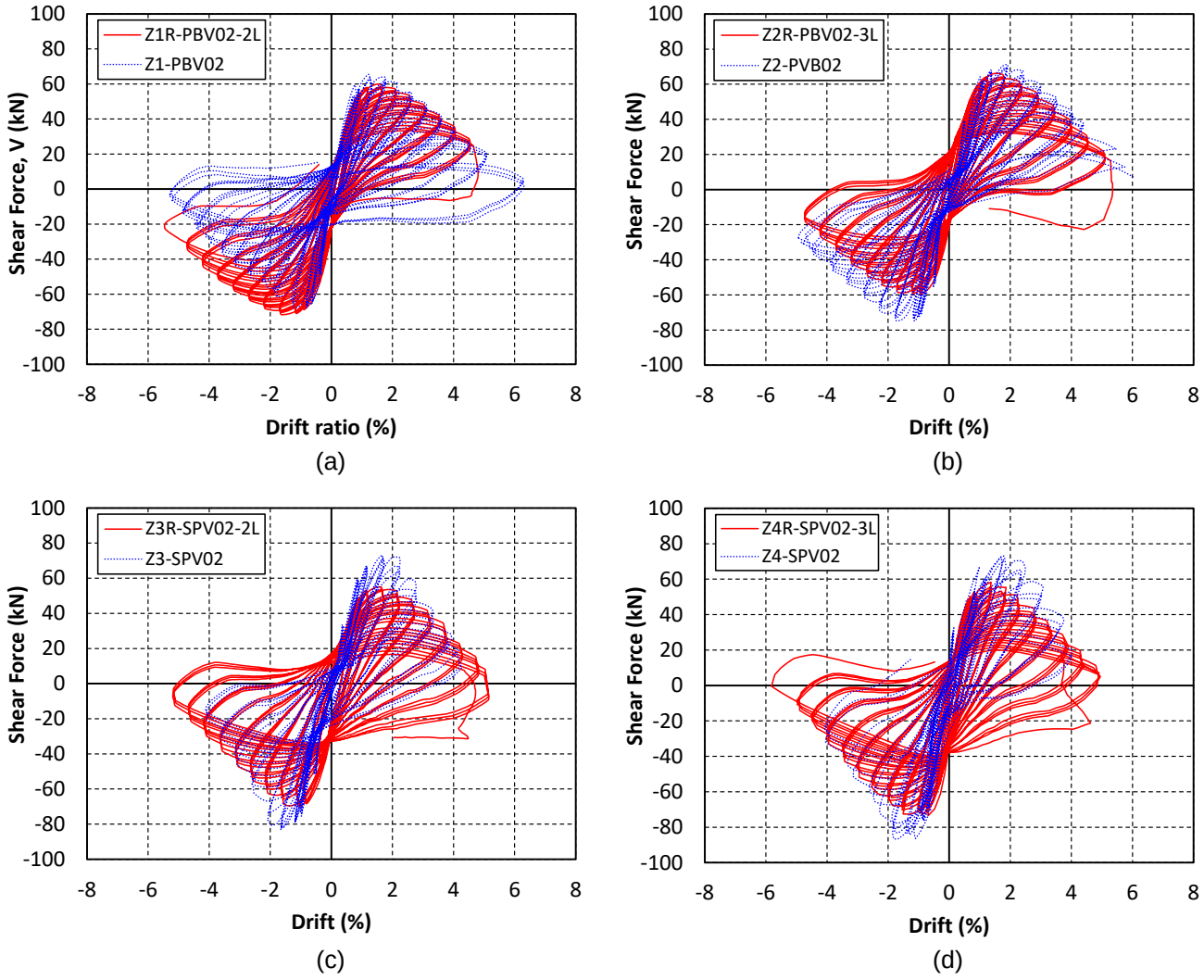

Figure 11: Comparison of experimental shear force – drift ratio curves between the as-built and the repaired specimens: (a) specimens Z1; (b) specimens Z2; (c) specimens Z3; (d) specimens Z4.

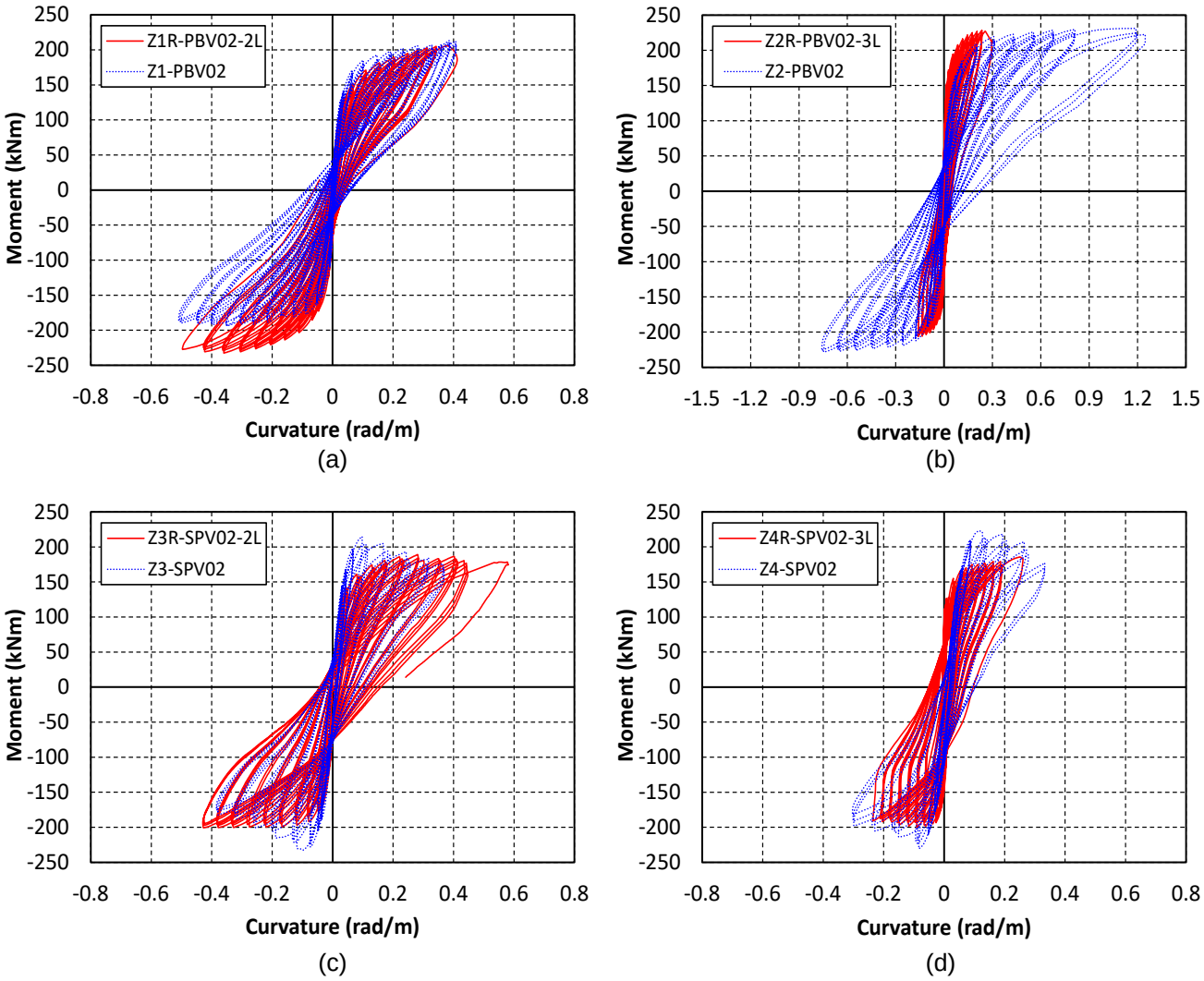

Figure 12: Comparison of experimental moment – curvature curves between the as-built and the repaired specimens: (a) specimens Z1; (b) specimens Z2; (c) specimens Z3; (d) specimens Z4.

Table 4 summarises the main experimental results.

Table 4: Summary of the experimental results.

Id	Specimen	V_{max} (kN)	$\frac{V_{max}}{b \cdot h \cdot f_c}$	Δ_{yl} (mm)	Δ_u (mm)	$\mu_{\Delta u}$	M_{max} (kN)	$\frac{M_{max}}{b \cdot h^2 \cdot f_c}$	φ_{yl} (10^{-3} rad/m)	φ_u (10^{-3} rad/m)	$\mu_{\varphi u}$	E_{sum} (kNm)	E_N	K_0 (kN/m)
1	Z1-PBV02 [13]	66.49	0.0082	14.92	51.49	3.45	203.08	0.096	58.35	407.57	6.98	27.91	14.31	4515.25
2	Z2-PBV02 [13]	72.19	0.0084	18.08	60.98	3.37	228.44	0.103	93.41	747.90	8.01	26.98	10.14	4537.94
3	Z3-SPV02 [13]	78.03	0.0095	20.36	49.64	2.44	223.55	0.104	47.14	364.36	7.73	25.82	10.91	4594.97
4	Z4-SPV02 [13]	79.83	0.0097	20.08	52.36	2.61	215.74	0.101	56.94	299.00	5.25	23.28	11.42	4208.88
5	Z1R-PBV02-2L	65.69	0.0081	17.18	62.77	3.65	218.56	0.103	80.09	382.24	4.77	32.08	15.28	4101.02
6	Z2R-PBV02-3L	61.96	0.0072	15.94	59.08	3.71	214.68	0.097	25.67	160.46	6.25	38.75	19.18	4089.02
7	Z3R-SPV02-2L	61.50	0.0075	15.55	54.86	3.53	194.30	0.091	43.89	426.33	9.71	44.86	27.96	3461.04
8	Z4R-SPV02-3L	65.48	0.0080	13.91	50.83	3.66	187.74	0.088	17.71	236.29	13.34	35.40	23.60	3496.00

4.2. Strength capacity.

Table 4 shows the relative maximum shear force $V_{max}/(f_c \cdot b \cdot h)$ and relative maximum bending moment in the critical section $M_{max}/(f_c \cdot b \cdot h^2)$ reached in each test, where f_c is the compressive strength of the UHPC precast column. In both cases, the self-weight effects were considered for calculating the bending moment and shear force. Second-order effects were also considered in calculating the bending moment. As expected, strength capacity $V_{max}/(f_c \cdot b \cdot h)$ was greater in the SP specimens (Z3-SPV02 and Z4-SPV02) because the joint between the column and the foundation had flexural tensile strength capacity, unlike the PB connection (Z1-PBV02 and Z2-PBV02). The maximum moment reached $M_{max}/(f_c \cdot b \cdot h^2)$ in the four specimens was similar because the flexural tensile strength capacity in the critical section was non-existent in the PB connections or was lower in SP specimens as the crack in the critical section widened.

In the repaired specimens (second test stage) the relative maximum shear force was similar in the four specimens (Figure 11), although the average behaviour of the SP specimens was slightly better. For the relative maximum bending moment (Figure 12), strength was greater in the PB specimens (ZR1-PBV02-2L and Z2R-PBV02-3L) due to less damage in the joint section than in the critical section of specimens ZR3-SPV02-2L and Z4R-SPV02-3L. No significant differences were found between the repairs with two or three CFRP layers. The failure mode of all specimens was due to instability as when they reached the maximum lateral load, the bearing bending moment continued to increase (specimens Z1R-PBV02-2L and Z2R-PBV02-3L) or the moment was constant (specimens Z3R-SPV02-2L and Z4R-SPV02-3L).

Comparing the strength capacity of the as-built specimens and repaired specimens, the relative maximum shear force $V_{max}/(f_c \cdot b \cdot h)$ did not recover after repair. A reduction of between 1.2% and 21.2% was found according to the damage involved. Reduction was greater in the SP specimens. The repair in column Z1-PBV02 increased its flexural strength $M_{max}/(f_c \cdot b \cdot h^2)$ by 7.7% because it had the least damage in the first stage test. In the other elements the bearing moment reduced by between 6% and 13%. The greatest reduction took place in the SP columns because they underwent more damage in the first stage.

4.3. Failure modes.

All the repaired specimens underwent instability failure. The bearing moment of the critical section remained constant (plastic moment) after the specimen reached the maximum lateral load (Z3R-SPV02-2L and Z4R-SPV02-3L, see Figure 12.c and d) or the moment even continued to increase (Z1R-PBV02-2L and Z2R-PBV02-3L, see Figure 12.a and b) indicating instability failure. In other words, the P-delta effect caused the second order moments to be large in the critical section to the point where they exceeded the section's plastic moment, so that the cyclic lateral load necessarily decreased. This also occurred in as-built PB specimens (Figure 12.a and b). However, these specimens reached the peak lateral load (Figure 11.c and d) when the critical section reached the peak moment (Figure 12.c and d), indicating material failure mode, specifically in the concrete. The repair thus changed the failure modes of specimens Z3R-SPV2-2L and Z4R-SPV02-3L from material failure to instability failure. The reason for this behaviour was that the bending cracking in the critical section was already present in the repaired SP connection specimens, so that the bending strength decreased and the moment remained plastic since the peak moment was reached.

4.4. Deformation capacity.

Figure 13 shows the idealisation of the actual envelope diagram [59,60] shear force-tip displacement ($V-\Delta$) or moment-curvature ($M-\varphi$) in a bilinear diagram made up of an elastic branch and a decreasing inelastic branch. The bilinear diagram can calculate the ultimate displacement ductility $\mu_{\Delta u}=\Delta_u/\Delta_{yI}$, where Δ_u is the ultimate displacement of the column at 0.80 of the maximum load on the descending branch, and Δ_{yI} is the effective elastic displacement. The ultimate curvature ductility is $\mu_{\varphi u}=\varphi_u/\varphi_{yI}$, where φ_u is the ultimate curvature of the section at 0.80 of the maximum moment on the descending branch, and φ_{yI} is the effective elastic curvature.

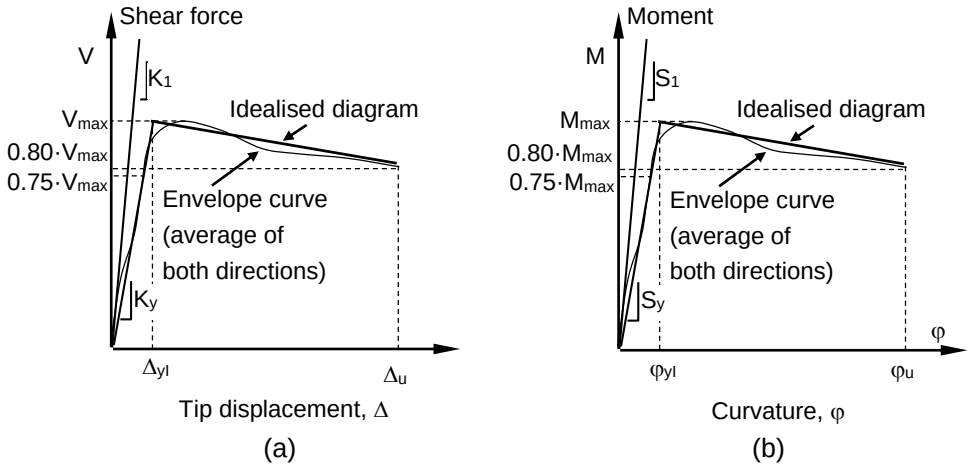

Figure 13: Ideal curve definitions [12].

Table 4 shows the ductility of each specimen. Except for Z3-SPV02 and Z4-SPV02, whose displacement ductility $\mu_{\Delta u}$ came close to 3 (high ductility according to NCSE-02 [61]), the displacement ductility of the other specimens was between high ($\mu_{\Delta u} = 3$) and very high ($\mu_{\Delta u} = 4$). It should be noted that the repaired specimens displayed greater displacement ductility $\mu_{\Delta u}$. The reason for this lies in the first test stage, because the joint between the column and the foundation opened, as found in the PB specimens (as-built or repaired), or because a crack opened in the critical zone in specimens. In Z1 and Z2, the mean ductility of the two as-built specimens was 3.41, while it was 3.68 in the repaired specimens, i.e. the repair recovered the original specimen's displacement ductility. The reason for this is that the strength of the epoxy resin between the column and the foundation was overcome in the first test stage, so that rocking behaviour occurred from the start. The strength capacity was thus slightly less in the repaired PB specimens, but ductility was slightly higher. In Z3 and Z4 (SP connection), the mean ductility of the two as-built specimens was 2.52, and that of the two repaired specimens was 3.60, as in Z1 and Z2. In the latter ductility improved because a crack in the critical section appeared in the first stage tests. This previous crack in Z3 and Z4 specimens behaved like the column-foundation joint of Z1 and Z2.

In the as-built SP specimen (Z3-SPV02 and Z4-SPV02) the flexural tensile strength of the critical section increased the strength capacity, but the degradation of this flexural tensile strength resulted in less ductility than in PB specimens. The repaired SP specimens (Z3-SPV02-2L and Z4-SPV02-

3L) had no flexural tensile strength in the critical section because of the previous cracking, so that strength was less although ductility was higher than the as-built specimens.

The displacement ductility in the specimens repaired with three CFRP wrapping layers was slightly greater than in the 2-layer specimens: 1.6% for PB and 3.7% for SP specimens. This behaviour was due to the larger number of reinforcement layers increasing the confinement in the critical zone, delayed the zone degradation and improving displacement ductility.

The repaired SP specimens had greater curvature ductility ($\mu_{\varphi u}$) (Table 4) than the as-built specimens. However, no conclusions were reached as to the PB specimens because the maximum bending moment value and 20% flexural capacity loss (descending branch) were not reached on the moment-curvature curve (Figure 12). The curvature ductility shown in Table 4 is thus a lower bound. Most specimens reached a higher curvature ductility value than expected if the conservative expression had been used that related both ductility values ($\mu_{\varphi u} = 2\mu_{\Delta u} - 1$) from EC-8 [62], except for Z1R-PB02-2L. The 3-layer specimens had greater curvature ductility than the 2..

4.5. Energy dissipation.

The energy dissipation of each j-cycle of the ith drift ratio hysteretic loop is defined as (Figure 14):

$$E_i^j = \oint_A^B V d\Delta \tag{1}$$

Total dissipated energy during the test can be expressed as:

$$E_{sum} = \sum_i^{m_1} \sum_j^{m_2} E_i^j \tag{2}$$

where E_{sum} is cumulate dissipated energy; m_1 the number of the drift ratio until the specimen loses 20% shear force, which is approximately a target drift of 3% and m_2 is the number of cycles for each drift ratio. To compare the elements' dissipated energy normalised dissipated energy E_N is calculated as [63]:

$$E_N = \sum_i^{m_1} \sum_j^{m_2} \left[E_i^j / \left(V_i^j \Delta_i^j\right)\right] \tag{3}$$

$$\Delta_i^j = \left(\left|\Delta_i^{j+}\right| + \left|\Delta_i^{j-}\right|\right)/2,\ V_i^j = \left(\left|V_i^{j+}\right| + \left|V_i^{j-}\right|\right)/2 \tag{4}$$

where Δ_i^{j+} and Δ_i^{j-} are the maximum displacements in the j[th] cycle in the i[th] drift ratio in the pull and the push direction, respectively; V_i^{j+} and V_i^{j-} are the shear forces of Δ_i^{j+} and Δ_i^{j-}, respectively.

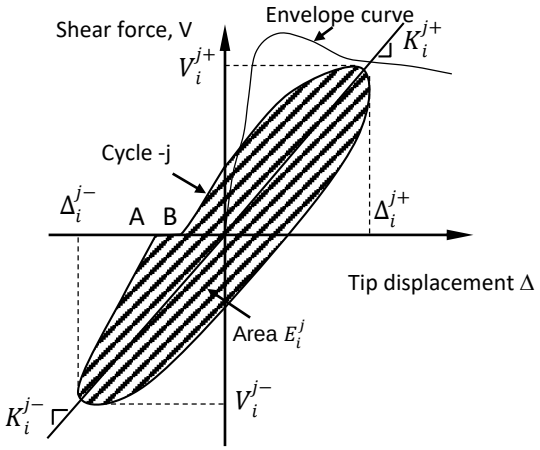

Figure 14: Energy dissipation [12].

Table 4 offers the results of the total dissipated energy and normalised energy of all the specimens. A similar amount of energy was dissipated in the as-built specimens for both connection types. More energy was dissipated in the repaired specimens than in the as-built specimens. The confined CFRP repair zone allowed more energy to be dissipated than in the as-built specimens. In this zone the degraded repair mortar and the CFRP wrapping prevented mortar spalling and allowed high strains to be reached. In the repaired SP specimens, an average increase of 131.5% of dissipated energy was observed, compared to the as-built specimens. In case of PB specimens, the average increase was 48.0%. When comparing SP and PB repaired specimens, more energy was dissipated by SP specimens (53% in average) because the repaired area in specimens Z3 and Z4 had a larger surface than in specimens Z1 and Z2. No significant differences were found in the repaired specimens by the number of CFRP layers.

4.6. Stiffness degradation.

The column stiffness (K_i) in the i[th] drift ratio is defined as [63]:

$$K_i = \sum_{j=1}^{m_2} V_i^j / \sum_{j=1}^{m_2} \Delta_i^j \quad (5)$$

where K_i is the mean secant stiffness at the i[th] drift ratio; Δ_i^j and V_i^j are defined in Equation (4). To compare the results, normalised column stiffness η_{K_i} is calculated by dividing by the stiffness for a drift ratio of 0.5% (K_0) at which the columns maintain an elastic behaviour.

$$\eta_{K_i} = K_i / K_0 \tag{6}$$

Table 4 shows the results of K_0. The mean stiffness K_0 value equal to 4,464.26 kN/m in the as-built specimens. The K_0 values were similar for each connection type (4526.6 kN/m for PB and 4401.93 kN/m for SP).

Stiffness K_0 was significantly reduced in the repaired specimens due to the damage caused during the tests on the as-built specimens (first test stage). The mean K_0 value in the repaired PB specimens was 4,095.02 kN/m (decrease of 9.5%), while it was 3,478.52 kN/m in the repaired SP specimens (decrease of 21%). More damage was noted in the critical section of SP specimens, which thus had the greatest reduction in stiffness K_0. This means that the proposed repair could not restore the specimen to its original K_0.

Figure 15 describes the normalized column stiffness η_{K_i} of all the samples according to the drift ratio. Before maximum shear force V_{max} was reached the PB specimens (Z1 and Z2) generally had lower relative stiffness. As the drift ratio increased, the bending moment of the critical section also increased in all the samples for the same axial load and the depth of the neutral axis decreased, which required greater curvature. The larger curvature in PB specimens meant that the normalised stiffness η_{K_i} was significantly reduced because there was no flexural tensile strength in the critical section of these specimens, unlike the SP (Z3 and Z4), which had flexural tensile stiffness in the critical section thanks to the steel fibres. However, this trend was reversed for drift ratios after the maximum shear force V_{max} was reached because the critical section of the SP specimens degraded. There were no significant differences for either the as-built or repaired specimens, or between the specimens repaired with two or three CFRP layers.

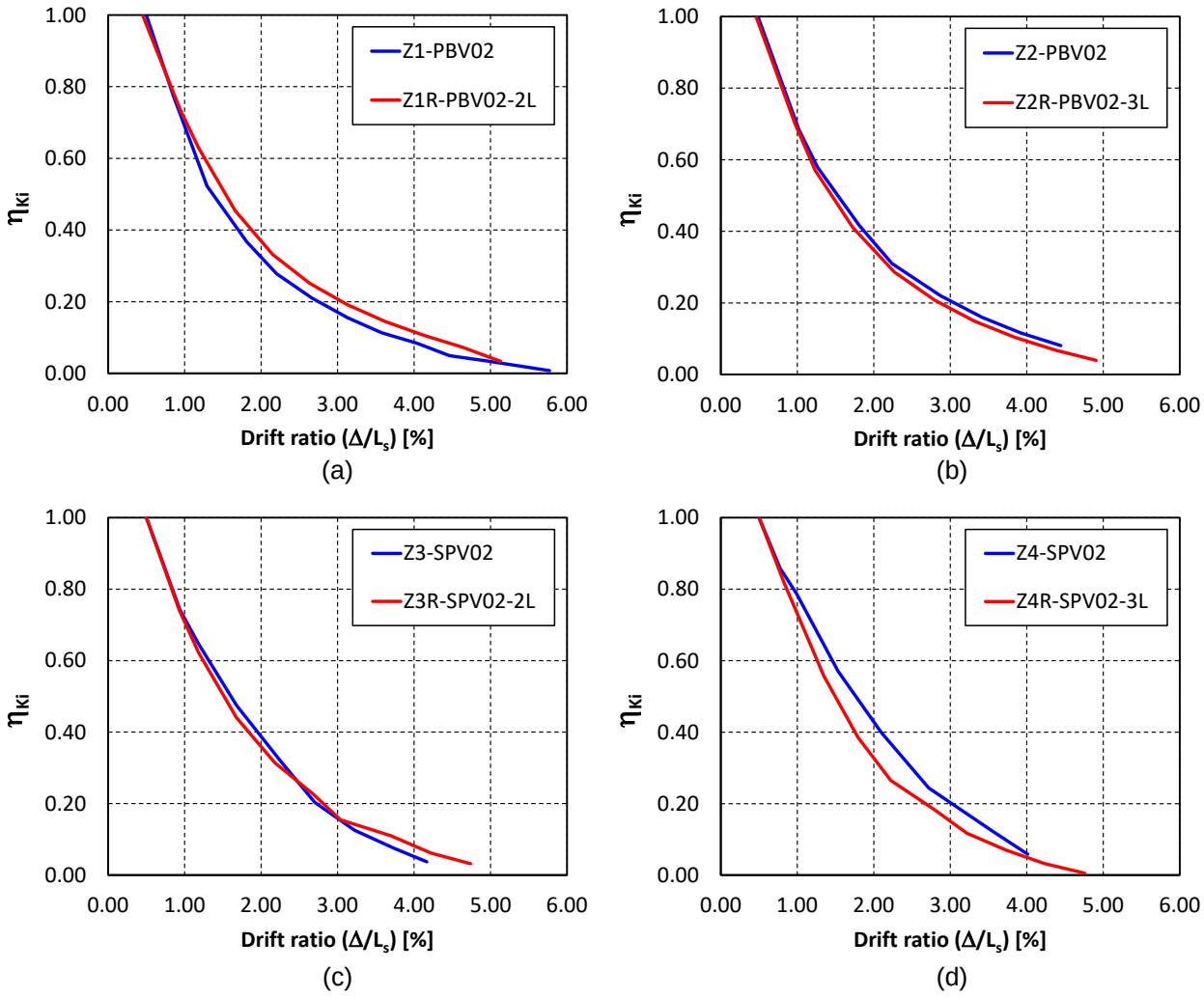

Figure 15: Comparison of the stiffness degradation between the as-built and the repaired specimens: (a) specimens Z1; (b) specimens Z2; (c) specimens Z3; (d) specimens Z4.

4.7. Residual drift ratio.

The mean residual drift ratio ($D_{r,i}$) of the column in the i[th] drift ratio is defined as:

$$D_{r,i} = \left(\left|D_{r,i}^{+}\right| + \left|D_{r,i}^{-}\right|\right)/2 \quad (7)$$

$$D_{r,i}^{+} = \sum_{j=1}^{m_2} D_{r,ij}^{+}/m_2 \; ; \; D_{r,i}^{-} = \sum_{j=1}^{m_2} D_{r,ij}^{-}/m_2 \quad (8)$$

where $D_{r,i}^{+}$ and $D_{r,i}^{-}$ are the average value of the residual drift ratio in the i[th] drift ratio in the pull and the push direction, respectively; $D_{r,ij}^{+}$ and $D_{r,i}^{-}$ are the residual drift ratio of the j[th] cycle at the i[th] drift ratio in the pull and the push direction, respectively; m_2 is the number of cycles of each i[th] drift ratio.

The mean residual drift ratio was analysed until the specimen displayed 20% shear force loss, which was approximately a 3% target drift.

Figure 16 shows the mean residual drift ratio of the column in the i^{th} drift ratio for all the specimens up to a drift ratio of between 3% and 4%. As we can see, in the as-built specimens the mean residual drift ratio values went below 0.5% for drift ratios below 2.5%. Up to this drift ratio, no significant differences had appeared between the different connections of the column with the foundation. In general, the mean residual drift ratio of the repaired specimens was higher than that of the as-built specimens due to the damage during the as-built specimens tests (first test stage). The mean residual drift ratio in the repaired specimens was less than 0.5% for drift ratios lower than 2.5% in the PB connection and for drift ratios lower than 1.5% in the SP connection, and was significantly lower in the PB specimens and about half that of the SP specimens for a 3% drift ratio. The lowest mean residual drift ratio was related to the lowest degradation of the critical section on the joint in the PB specimens (Z1 and Z2) compared to the damage noted in the critical section in the SP specimens (Z3 and Z4); see Figure 10.

The reduced residual deformations in the column resulted in the structure having a self-centring capacity. This behaviour was because the damage in UHPC was slight due to the super-elastic Ni-Ti SMA bars and the behaviour of CFRP wrapping.

4.8. Gap opening displacement in the joint between the column and foundation.

In all the PB specimens (Z1 and Z2), four LVDTs (devices 24-27) recorded possible joint displacement (Figure 8.b). Figure 17 gives an example of the displacements in specimen Z2, as-built and repaired the LVDTs for the different drift ratios (Δ/L_s). This figure has a linear interpolation for each drift ratio which gave sufficient approximation ($R^2 \approx 1$) to represent the strain plane. Rocking movement of the joint can be seen in the pull and push direction of the lateral load, with a large gap opening of > 6 mm in some cases. As expected, the compressive zone depth decreased as target drift increased. The changes in the neutral axis depth through this gap opening and the development of non-linear-inelastic compressive concrete behaviour caused moment-rotation connection behaviour without causing any significant damage or strength degradation. This was caused

because: (1) the bond loss of the Ni-Ti SMA bars that distributed the strain along the entire rebar; and (2) their highly ductile behaviour; (3) the use of high-fibre UHPC and high-performance repair mortar confined by CFRP wrapping.

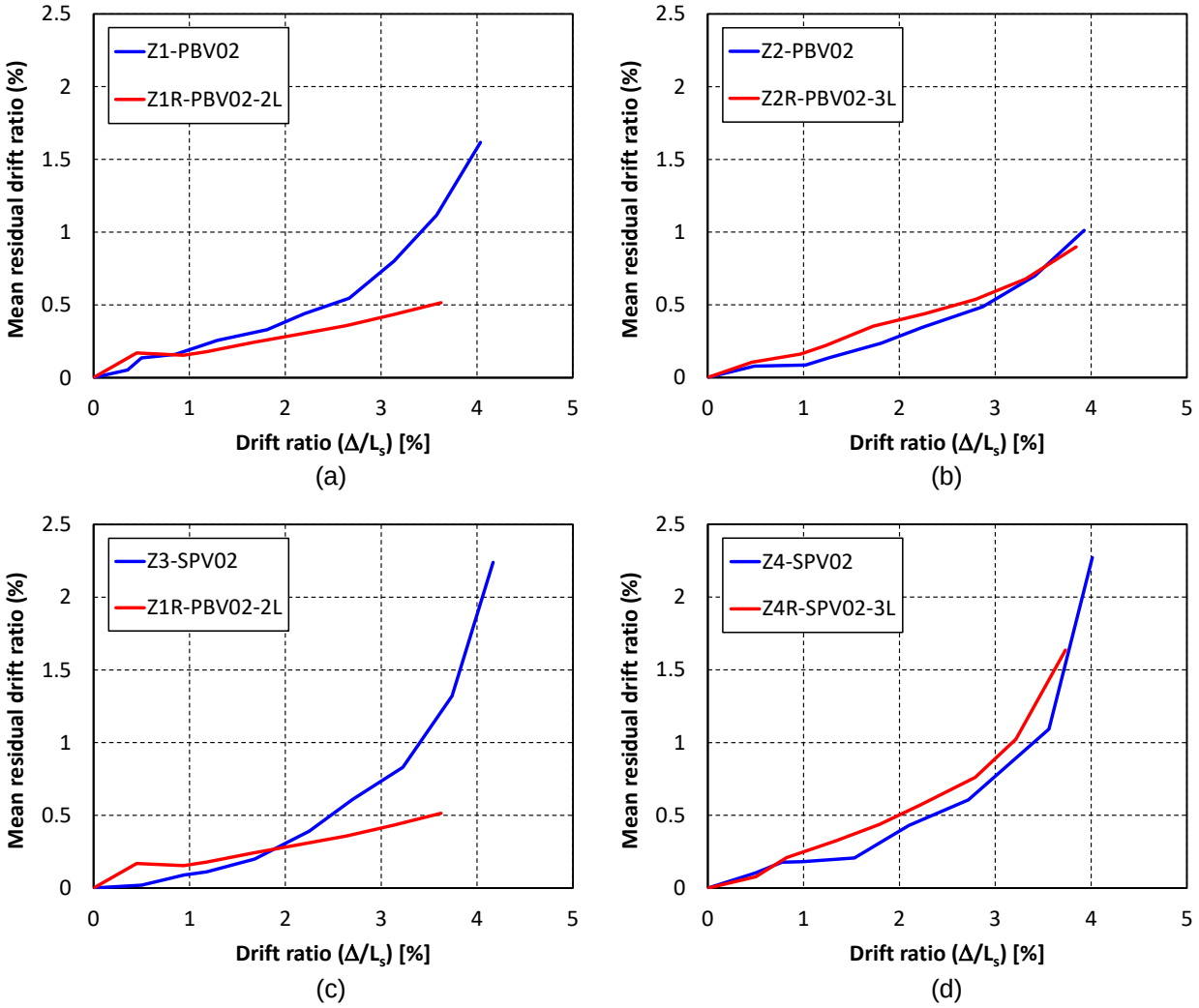

Figure 16: Comparison of the residual drift ratio between the as-built and the repaired specimens: (a) specimens Z1; (b) specimens Z2; (c) specimens Z3; (d) specimens Z4.

If the lateral load was zero, the joint remained compressed due to the recovery of the Ni-Ti bars (super-elasticity) and also because the concrete or repair mortar did not show any significant degradation in the joint. The high steel-fibre content in the UHPC and the high-performance confined repair mortar helped to achieve a significant compressive strain.

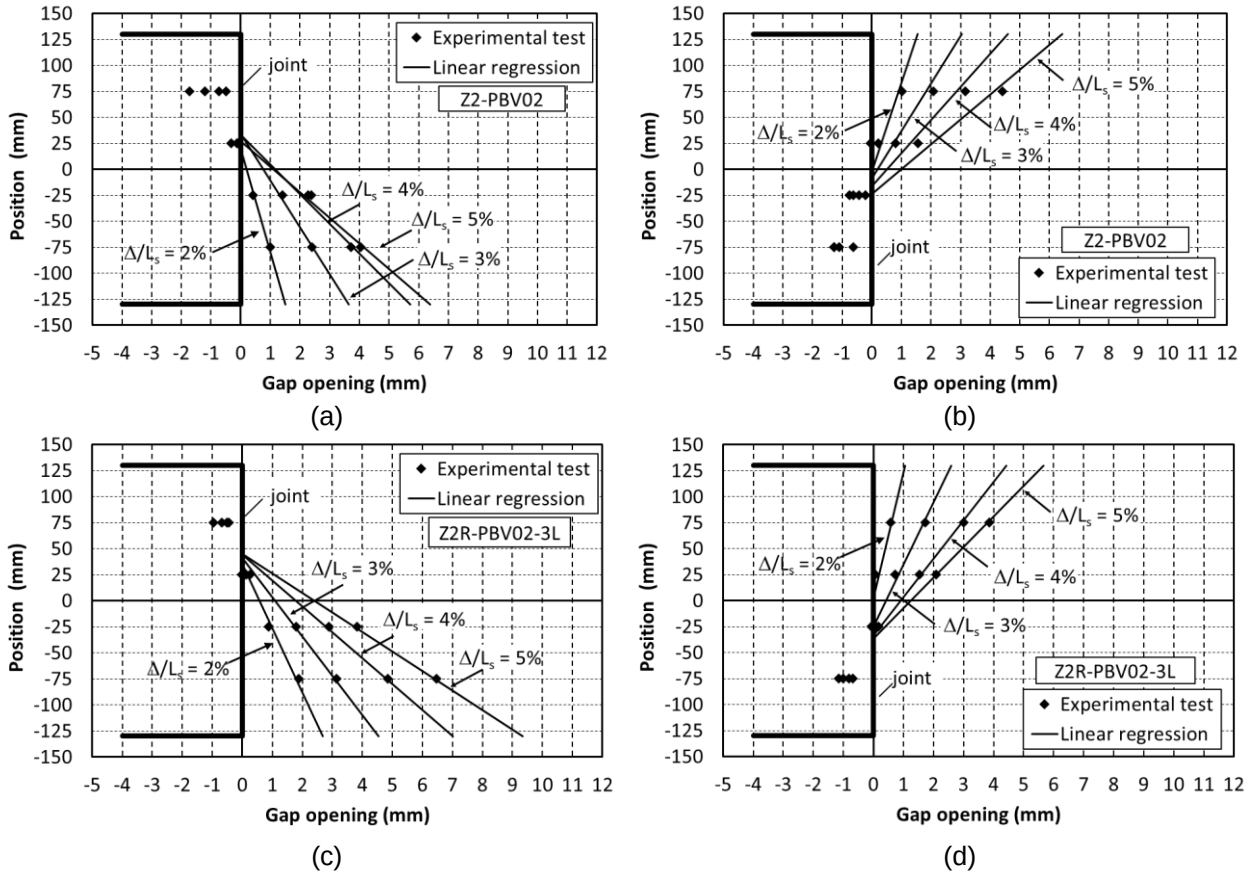

Figure 17: Gap opening displacement in the joint between the column and the foundation (specimen Z2).

5. Conclusions.

1. The repair with CFRP wrapping prevented the cover spalling of the repair mortar and confined both UHPC and the high-performance mortar, which allowed a significant compressive strain to be achieved. In the second test stage no local failure of the CFRP wrapping occurred.

2. In the specimens repaired with a PB connection, rocking behaviour occurred at the column/foundation joint due to: (1) the CFRP confinement allowed the UHPC and high-strength mortar to achieve significant compressive strains without concrete crushing; (2) the adequate tensile and compressive behaviour of the Ni-Ti SMA bars; (3) the reduced bond between the Ni-Ti SMA bars and UHPC, which enabled a significant tensile strain which did not concentrate in the joint. In these specimens repair did not restore strength capacity $V_{max}/(f_c \cdot b \cdot h)$. The average reduction was 8%, but displacement ductility $\mu_{\Delta u}$ rose by 8%. Due to the damage in these specimens in the first

test stage, dissipated energy E_N was higher and initial stiffness K_0 was lower in the second test stage.

3. The behaviour of the repaired SP specimens was conditioned by the main crack in the first test stage, where damage was concentrated. Although the specimens were repaired, there was a visible bending crack in the CFRP wrapping. In these specimens the critical section of the column with the bending crack displayed rocking behaviour. The adequate CFRP confinement allowed the UHPC and repair mortar to achieve significant compressive strains. In these specimens more damage appeared in the critical zone than in the repaired PB specimens due to CFRP bulging. The repair to these specimens did not restore their strength $V_{max}/(f_c \cdot b \cdot h)$, with an average 19% reduction due to the degraded flexural tensile strength in the critical section in the first test stage. However, displacement ductility $\mu_{\Delta u}$ improved by an average of 42% due to the prior crack, which allowed moment-rotation behaviour without increasing damage. Dissipated energy E_N rose but initial stiffness K_0 was lower in the second test stage because of the damage in the first test stage.

4. The mean residual drift ratio of the repaired specimens was higher because of the prior damage caused in the as-built specimen tests, so that the mean residual drift ratio in the repaired specimens was less than 0.5% for drift ratios below 2.5% for a PB connection and 1.5% for an SP connection. The lower mean residual drift ratio was related to the lesser degree of degradation of the critical section in the as-built specimens.

5. There were no significant differences between the 2 and 3 repair layers in relation to strength capacity, energy dissipation or E_N, or the initial stiffness K_0 value. However, the 3-layer specimens showed greater displacement and curvature as the damage in the critical zone decreased with the number of CFRP wrapping layers.

As a future research work, an optimization in the design would be proposed where the length of the SMA bars would be minimized. The optimization would also include different concrete types in the same column. UHPC would be employed where the plastic hinge was formed and the rest of the column would be made of another less expensive concrete. The mechanical properties of this

secondary concrete should be analyzed to assure the failure is not produced in this concrete, but in UHPC and SMA zone.

6. Acknowledgements.

This paper forms part of a line of research carried out at the University Institute of Concrete Science and Technology (ICITECH) of the Universitat Politècnica de València. The authors wish to thank the Spanish Ministry of Science and Innovation for the support provided through Projects BIA2012-32645 and RTI2018-099091-B-C21-AR, and Grant BES-2016-078010 from the European Union for the financial support with FEDER funds, and the Spanish Ministry of Education, Culture and Sport for Grant FPU12/01451.

References

[1] J. Wang, S. Lu, J. Yang, Behavior of eccentrically loaded rectangular RC columns wrapped with CFRP jackets under different preloading levels, J. Build. Eng. 34 (2021). https://doi.org/10.1016/j.jobe.2020.101943.

[2] L. Lam, J.G. Teng, Design-oriented stress–strain model for FRP-confined concrete, Constr. Build. Mater. 17 (2003) 471–489. https://doi.org/10.1016/S0950-0618(03)00045-X.

[3] N.A. Siddiqui, S.H. Alsayed, Y.A. Al-Salloum, R.A. Iqbal, H. Abbas, Experimental investigation of slender circular RC columns strengthened with FRP composites, Constr. Build. Mater. 69 (2014) 323–334. https://doi.org/10.1016/j.conbuildmat.2014.07.053.

[4] B. Ferracuti, M. Savoia, M. Zucconi, RC frame structures retrofitted by FRP-wrapping: A model for columns under axial loading and cyclic bending, Eng. Struct. 207 (2020) 110243. https://doi.org/10.1016/j.engstruct.2020.110243.

[5] C. Dundar, D. Erturkmen, S. Tokgoz, Studies on carbon fiber polymer confined slender plain and steel fiber reinforced concrete columns, Eng. Struct. 102 (2015) 31–39. https://doi.org/10.1016/j.engstruct.2015.08.011.

[6] J. Shin, D.W. Scott, L.K. Stewart, C.S. Yang, T.R. Wright, R. DesRoches, Dynamic response of a full-scale reinforced concrete building frame retrofitted with FRP column jackets, Eng. Struct. 125 (2016) 244–253. https://doi.org/10.1016/j.engstruct.2016.07.016.

[7] M. Quiertant, J.-L. Clement, Behavior of RC columns strengthened with different CFRP systems under eccentric loading, Constr. Build. Mater. 25 (2011) 452–460. http://www.scopus.com/inward/record.url?eid=2-s2.0-78649823072&partnerID=tZOtx3y1 (accessed November 12, 2015).

[8] P. Faustino, P. Frade, C. Chastre, Lateral Cyclic Behaviour of RC Columns Confined With Carbon Fibres, ISTRUC. 5 (2016) 196–206. https://doi.org/10.1016/j.istruc.2015.11.004.

[9] Y.S. Youcef, S. Amziane, M. Chemrouk, CFRP confinement effectiveness on the behavior of reinforced concrete columns with respect to buckling instability, Constr. Build. Mater. 81 (2015) 81–92. https://doi.org/10.1016/j.conbuildmat.2015.02.006.

[10] A. Romero-García, J.L. Bonet, J.R. Martí-Vargas, J. Navarro-Gregori, Behaviour of precast columns to-foundation connections under cyclic loading, 15th World Conf. Earthq. Eng. (2012) 24–28.

[11] J. Pereiro-Barceló, J.L. Bonet, B. Cabañero-Escudero, B. Martínez-Jaén, Cyclic behavior of hybrid RC columns using High-Performance Fiber-Reinforced Concrete and Ni-Ti SMA bars in critical regions, Compos. Struct. 212 (2019) 207–219. https://doi.org/10.1016/j.compstruct.2019.01.029.

[12] J. Pereiro-Barceló, J.L. Bonet, S. Gómez-Portillo, C. Castro-Bugallo, Ductility of high-

performance concrete and very-high-performance concrete elements with Ni-Ti reinforcements, Constr. Build. Mater. 175 (2018) 531–551. https://doi.org/10.1016/j.conbuildmat.2018.04.172.
[13] J. Pereiro-Barceló, J.L. Bonet, L. Rueda-García, J.R. Albiol-Ibáñez, Cyclic response of precast column-to-foundation connection using UHPC and Ni-Ti SMA reinforcements in columns (Draft), Eng. Struct. (2021).
[14] ASTM C1856 / C1856M - 17: Standard Practice for Fabricating and Testing Specimens of Ultra-High Performance Concrete, (n.d.).
[15] V.H. (Vic). Perry, What Really Is Ultra-High Performance Concrete - Towards a Global Definition, 2018.
[16] J.C. Walraven, High performance fiber reinforced concrete: Progress in knowledge and design codes, Mater. Struct. Constr. 42 (2009) 1247–1260. https://doi.org/10.1617/s11527-009-9538-3.
[17] I. Markovic, High-Performance Hybrid-Fibre Concrete: Development and Utilisation, DUP Science, Delft, 2006.
[18] N. Naeimi, M.A. Moustafa, Numerical modeling and design sensitivity of structural and seismic behavior of UHPC bridge piers, Eng. Struct. 219 (2020) 110792. https://doi.org/10.1016/j.engstruct.2020.110792.
[19] J. Xue, B. Briseghella, F. Huang, C. Nuti, H. Tabatabai, B. Chen, Review of ultra-high performance concrete and its application in bridge engineering, Constr. Build. Mater. 260 (2020). https://doi.org/10.1016/j.conbuildmat.2020.119844.
[20] C.-C. Hung, C.-H. Yen, Compressive behavior and strength model of reinforced UHPC short columns, J. Build. Eng. 35 (2021). https://doi.org/10.1016/j.jobe.2020.102103.
[21] J. Walraven, High performance concrete: A material with a large potential, J. Adv. Concr. Technol. 7 (2009) 145–156. https://doi.org/10.3151/jact.7.145.
[22] C. Castro, Análisis experimental de soportes de hormigón de altas prestaciones sometidos a compresión y carga lateral cíclica, Universitat Politècnica de València, 2016.
[23] G.L. Guerrini, Applications of High-Performance Fiber-Reinforced Cement-Based Composites, Appl. Compos. Mater. 7 (2000) 195–207.
[24] W. Pansuk, T.N. Nguyen, Y. Sato, J.A. Den Uijl, J.C. Walraven, Shear capacity of high performance fiber reinforced concrete I-beams, Constr. Build. Mater. 157 (2017) 182–193. https://doi.org/10.1016/j.conbuildmat.2017.09.057.
[25] N. Naeimi, M.A. Moustafa, Compressive behavior and stress–strain relationships of confined and unconfined UHPC, Constr. Build. Mater. 272 (2021). https://doi.org/10.1016/j.conbuildmat.2020.121844.
[26] W. Zhu, J. Jia, J. Gao, F. Zhang, Experimental study on steel reinforced high-strength concrete columns under cyclic lateral force and constant axial load, Eng. Struct. 125 (2016) 191–204. https://doi.org/10.1016/j.engstruct.2016.07.018.
[27] X. Zeng, K. Deng, H. Liang, R. Xu, C. Zhao, B. Cui, Uniaxial behavior and constitutive model of reinforcement confined coarse aggregate UHPC, Eng. Struct. 207 (2020) 110261. https://doi.org/10.1016/j.engstruct.2020.110261.
[28] S.T. Kang, Y. Lee, Y.D. Park, J.K. Kim, Tensile fracture properties of an Ultra High Performance Fiber Reinforced Concrete (UHPFRC) with steel fiber, Compos. Struct. 92 (2010) 61–71. https://doi.org/10.1016/j.compstruct.2009.06.012.
[29] Z. Wang, J. Wang, G. Zhao, J. Zhang, Design criterion for the self-centering capacity of precast segmental UHPC bridge columns with unbonded post-tensioning tendons, Eng. Struct. 200 (2019) 109706. https://doi.org/10.1016/j.engstruct.2019.109706.
[30] J. Pereiro-Barceló, J.L. Bonet, J.R. Albiol-Ibáñez, Buckling of steel and Ni-Ti reinforcements in very high performance concrete (VHPC) elements, Constr. Build. Mater. 160 (2018) 551–563. https://doi.org/10.1016/j.conbuildmat.2017.11.113.
[31] Y. Zhang, P. Zhu, J. Shi, Flexural behavior of precast UHPC beam with prestressed bolted hybrid joint, Eng. Struct. 206 (2020) 110100. https://doi.org/10.1016/j.engstruct.2019.110100.
[32] G. Zhang, Q. Han, K. Xu, X. Du, W. He, Experimental investigation of seismic behavior of UHPC-filled socket precast bridge column-foundation connection with shear keys, Eng. Struct. (2020). https://doi.org/10.1016/j.engstruct.2020.111527.
[33] R. DesRoches, M. Delemont, Seismic retrofit of simply supported bridges using shape memory

alloys, Eng. Struct. 24 (2002) 325–332. https://doi.org/10.1016/S0141-0296(01)00098-0.
[34] M.S. Alam, M.A. Youssef, M. Nehdi, Analytical prediction of the seismic behaviour of superelastic shape memory alloy reinforced concrete elements, Eng. Struct. 30 (2008) 3399–3411. https://doi.org/10.1016/j.engstruct.2008.05.025.
[35] A.H.M.M. Billah, M.S. Alam, Probabilistic seismic risk assessment of concrete bridge piers reinforced with different types of shape memory alloys, Eng. Struct. 162 (2018) 97–108. https://doi.org/10.1016/j.engstruct.2018.02.034.
[36] M.S. Alam, M. Nehdi, M.A. Youssef, Seismic performance of concrete frame structures reinforced with superelastic shape memory alloys, Smart Struct. Syst. 5 (2009) 565–585. https://doi.org/10.12989/sss.2009.5.5.565.
[37] M.S. Alam, M. Moni, S. Tesfamariam, Seismic overstrength and ductility of concrete buildings reinforced with superelastic shape memory alloy rebar, Eng. Struct. 34 (2012) 8–20. https://doi.org/10.1016/j.engstruct.2011.08.030.
[38] A.H.M.M. Muntasir Billah, M. Shahria Alam, Seismic performance of concrete columns reinforced with hybrid shape memory alloy (SMA) and fiber reinforced polymer (FRP) bars, Constr. Build. Mater. 28 (2012) 730–742. https://doi.org/10.1016/j.conbuildmat.2011.10.020.
[39] S. Jiang, Y. Zhang, Microstructure evolution and deformation behavior of as-cast NiTi shape memory alloy under compression, Trans. Nonferrous Met. Soc. China. 22 (2012) 90–96. https://doi.org/10.1016/S1003-6326(11)61145-X.
[40] C.X. Qiu, S. Zhu, Characterization of cyclic properties of superelastic monocrystalline Cu-Al-Be SMA wires for seismic applications, Constr. Build. Mater. 72 (2014) 219–230. https://doi.org/10.1016/j.conbuildmat.2014.08.065.
[41] K.C. Shrestha, M.S. Saiidi, C.A. Cruz, Advanced materials for control of post-earthquake damage in bridges, Smart Mater. Struct. 24 (2015) 25035. https://doi.org/10.1088/0964-1726/24/2/025035.
[42] M.S. Saiidi, M. Tazarv, B. Nakashoji, S. Varela, F. Kavianipour, Resilient and Sustainable Bridges of the Future, Int. J. Bridg. Eng. 3 (2015) 37–48.
[43] J.L. Bonet, J. Pereiro-Barceló, A. Navarro-Gómez, Elemento de Conexión de Protección Contra Sismos: P201631022, 2017.
[44] AENOR, UNE-EN 12390-3:2020 Ensayos de hormigón endurecido. Parte 3: D..., (n.d.). https://www.une.org/encuentra-tu-norma/busca-tu-norma/norma?c=N0063272 (accessed December 12, 2020).
[45] A.S.A. for S. and Certification, UNE-EN 14651:2007+A1:2008. Test method for metallic fibre concrete - Measuring the flexural tensile strength (limit of proportionality (LOP), residual), (2017). http://www.aenor.es/aenor/normas/normas/fichanorma.asp?tipo=N&codigo=N0041225#.WphGrnxG2Uk.
[46] M. Fomento, Instrucción de Hormigón Estructural (EHE-08), 2008.
[47] BS EN 1992-1-1, Eurocode 2: Design of concrete structures - Part 1-1 : General rules and rules for buildings, 2004. https://doi.org/[Authority: The European Union Per Regulation 305/2011, Directive 98/34/EC, Directive 2004/18/EC].
[48] AENOR, UNE-EN 10002-1:2002 Materiales metálicos. Ensayos de tracción...., (n.d.). https://www.une.org/encuentra-tu-norma/busca-tu-norma/norma/?c=N0027411 (accessed December 12, 2020).
[49] ASTM F2004 - 05(2010) Standard Test Method for Transformation Temperature of Nickel-Titanium Alloys by Thermal Analysis, (n.d.). https://www.astm.org/DATABASE.CART/HISTORICAL/F2004-05R10.htm (accessed December 12, 2020).
[50] Y.L. Mo, J. Chan, Bond and slip of plain rebars in concrete, J. Mater. Civ. Eng. 8 (1996) 208–211. https://doi.org/10.1061/(ASCE)0899-1561(1996)8:4(208).
[51] G.M. Verderame, G. De Carlo, P. Ricci, G. Fabbrocino, Cyclic bond behaviour of plain bars. Part II: Analytical investigation, Constr. Build. Mater. 23 (2009) 3512–3522. https://doi.org/10.1016/j.conbuildmat.2009.07.001.
[52] AENOR, UNE-EN 12390-13:2014 Ensayos de hormigón endurecido. Parte 13:..., Aenor. (2014). https://www.une.org/encuentra-tu-norma/busca-tu-norma/norma/?c=N0053157 (accessed December 12, 2020).

[53] Y.A. Al-Salloum, Influence of edge sharpness on the strength of square concrete columns confined with FRP composite laminates, Compos. Part B Eng. 38 (2007) 640–650. https://doi.org/10.1016/j.compositesb.2006.06.019.
[54] ACI Committee 374, Acceptance Criteria for Moment Frames Based on Structural Testing and Commentary, 2005.
[55] FEMA 356, FEMA 356 - Prestandard and commentary for the seismic rehabilitation of buildings , FEDERAL EMERGENCY MANAGEMENT AGENCY, 2000. http://scholar.google.com/scholar?hl=en&btnG=Search&q=intitle:Prestandard+and+commentary+for+the+seismic+rehabilitation+of+buildings#0 (accessed December 12, 2020).
[56] FEMA 750, NEHRP (National Earthquake Hazards Reduction Program) Recommended Seismic Provisions for New Buildings and Other Structures (FEMA P-750), 2009 Edition, 2009. www.bssconline.org (accessed December 12, 2020).
[57] R. Park, Simulated seismic load tests on reinforced concrete elements and structures, in: Earthq. Eng. Tenth World Conf., Balkema, Rotterdam, 1994: pp. 6681–6693.
[58] J. Liu, Seismic Behaviour of Reinforced Concrete Columns, University of Toronto, 2013.
[59] J.C.M. Ho, H.J. Pam, Inelastic design of low-axially loaded high-strength reinforced concrete columns, Eng. Struct. 25 (2003) 1083–1096. https://doi.org/10.1016/S0141-0296(03)00050-6.
[60] P. Paultre, M. Boucher-Trudeau, R. Eid, N. Roy, Behavior of Circular Reinforced-Concrete Columns Confined with Carbon Fiber–Reinforced Polymers under Cyclic Flexure and Constant Axial Load, J. Compos. Constr. 20 (2016) 04015065. https://doi.org/10.1061/(asce)cc.1943-5614.0000624.
[61] Ministry of Development, Norma de Construcción Sismorresistente: Parte general y edificación (NCSE-02), 2013. https://doi.org/10.1017/CBO9781107415324.004.
[62] CEN, Eurocode 8 - Design of structures for earthquake resistance - Part 1: General rules, seismic actions and rules for buildings, Revisión U, ----------, 2005. https://doi.org/[Authority: The European Union per Regulation 305/2011, Directive 98/34/EC, Directive 2004/18/EC].
[63] W. Zhu, J. Jia, J. Gao, F. Zhang, Experimental study on steel reinforced high-strength concrete columns under cyclic lateral force and constant axial load, Eng. Struct. 125 (2016) 191–204. https://doi.org/10.1016/j.engstruct.2016.07.018.